Closed-Form Differential Kinematics for Concentric-Tube Continuum Robots with Application to Visual Servoing

R. J. Webster III[1], J. P. Swensen[3], J. M. Romano[2], and N. J. Cowan[3]

[1] Vanderbilt University, Nashville, TN, USA `robert.webster@vanderbilt.edu`
[2] University of Pennsylvania, Philadelphia, PA, USA `jrom@seas.upenn.edu`
[3] Johns Hopkins University, Baltimore, MD, USA {`jpswensen,ncowan`}`@jhu.edu`

Summary. Active cannulas, so named because of their potential medical applications, are a new class of continuum robots consisting of precurved, telescoping, elastic tubes. As individual component tubes are actuated at the base relative to one another, an active cannula changes shape to minimize stored elastic energy. For the first time, we derive the differential kinematics of a general n tube active cannula while accounting for torsional compliance, which can strongly affect the accuracy of robot tip pose prediction. Our derivation makes several explicit assumptions that have never been vetted for a robotic task, so we experimentally validate the Jacobian using a three-link prototype in a simple stereo visual servoing scheme. Our visual servoing experiments validate the Jacobian and also demonstrate the feasibility of using active cannulas under image guidance—a key step toward realizing their potential to reach dexterously through small, winding environments, which is of particular importance in medical applications.

1 Introduction

Continuum robots promise better maneuverability than traditional rigid-link robots in cluttered or unstructured environments, and their inherent compliance renders them gentler to objects they encounter. These features are particularly well-suited for minimally invasive surgery (MIS), where tools must traverse winding entry passages and maintain dexterity. However, applying continuum robots in MIS requires designing them to have small diameters without sacrificing dexterity. The active cannula [15] is a continuum robot design created with such criteria in mind. An active cannula is made from concentric, precurved, elastic component tubes (See Figure 1). It changes shape as tubes are axially translated and rotated with respect to each other, and consequently elastically interact. Since the curvature that enables bending is built into the backbone of the device itself (rather than e.g. tendon wires attached to support discs), active cannulas can be very thin and dexterous.

The potential of active cannulas in a wide variety of medical applications has been noted in [3, 4, 8, 13–15] and a review of potential applications is provided in [11]. The most compelling of these may be access deep within the lung via the throat.

Initial active cannula research has focused on kinematic modeling, applying beam mechanics to describe cannula shape [8, 9, 13–15]. Using this kinematic information to control the tip of the active cannula, as would be needed for virtually any of the previously suggested medical applications, would be greatly facilitated by deriving a parsimonious expression for the active cannula Jacobian matrix. Pure bending models that neglect torsional compliance [8, 9] provide a good starting point, because in this setting active cannula forward kinematics can be written in closed form and differentiated to produce a Jacobian. However, three of the current authors recently reported that neglecting torsional compliance can in some circumstances produce substantial errors between model predictions and actual cannula shape [14, 15]. Including these effects significantly improves the predictive power of the model, but it also leads to transcendental equations that must be numerically solved when computing the forward kinematics—much less the inverse or differential kinematics! Fortunately, however, all is not lost: we show that a closed-form Jacobian can be formulated via the minimum potential energy hypothesis, given the forward kinematic solution derived in [15] for a cannula with a torsionally compliant transmission. We then demonstrate experimentally that this Jacobian can be used to facilitate a simple visual servoing task.

2 Related Work

Continuum robots are characterized by a continuously flexible structure that often includes a backbone. Many innovative designs for transmitting bending moments to the structure have been proposed (see e.g. [7, 11] for overviews), including tendons, pneumatic chambers, or flexible push rods. The active can-
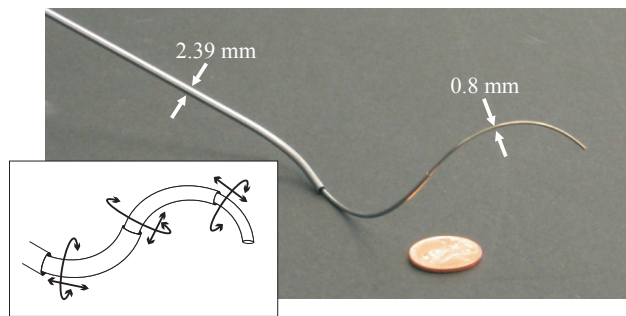

Fig. 1. A prototype active cannula made of super-elastic Nitinol tubes. The inset line drawing indicates degrees of freedom. This figure reprinted from [14].

nula uses the backbone itself to transmit bending moments via component tube elastic interaction. This allows active cannulas to be very thin, and dexterity improves with miniaturization [15]. Active cannulas were inspired by research on needle steering [12].[4]

Early designs with some similarity to active cannulas used fully overlapping precurved tubes which were rotated (but not translated) with respect to one another [4, 10]. A similar device that deploys a curved "catheter" through a rigid curved outer cannula has also been patented [2]. Beam-mechanics-based models accounting for the effects of both translation and rotation of component tubes were first presented by our group [13–15] and by Sears and Dupont [8, 9]. A distinction between the two similar modeling frameworks is the inclusion of transmissional torsion in [13–15]. Set-point regulation using a single fixed camera has been accomplished for hyper-redundant manipulators [1], but the authors are aware of no prior results on visual servoing for active cannulas or similar devices.

3 Differential Kinematics for an Active Cannula

Active cannulas are modeled as having piecewise constant curvature in [15]. The kinematic framework of [15], briefly reviewed in Section 3.1, provides arc parameters for curvature, plane, and arc length of each active cannula link, as functions of the active cannula joint variables. This Jacobian derivation (not previously reported) then proceeds in Section 3.2 in two steps. First, we derive the Jacobian from arc parameters to end-effector velocities; this is a general result applicable to any piecewise circular robot. Then we compute the arc parameter derivatives of the active cannula, in particular.

3.1 Review of Forward Kinematics

For reader convenience, we review the computation of the forward kinematics of an active cannula, reported in [15]. Active cannula joint space is parametrized by axial rotations, $\boldsymbol{\alpha}$, and translations, $\boldsymbol{\rho}$, applied at tube bases, namely $\boldsymbol{q} = (\alpha_1, \rho_1, \ldots, \alpha_n, \rho_n)$. In what follows, the subscript $i \in \{1, \ldots, n\}$ refers to tube number, while $j \in \{1, \ldots, m\}$ refers to link number. Cannula links are circular segments described by the arc parameters curvature, plane, and arc length $(\kappa_j, \phi_j, \ell_j)$, as shown in Figure 2. The kinematics of continuum robots can be decomposed into a mapping from joint space to arc parameters, and a mapping from arc parameters to shape.

Mapping From Joint Space to Arc Parameters

Consider an active cannula where each component tube has an initial straight section and a circularly precurved tip. The shape of the active cannula is then
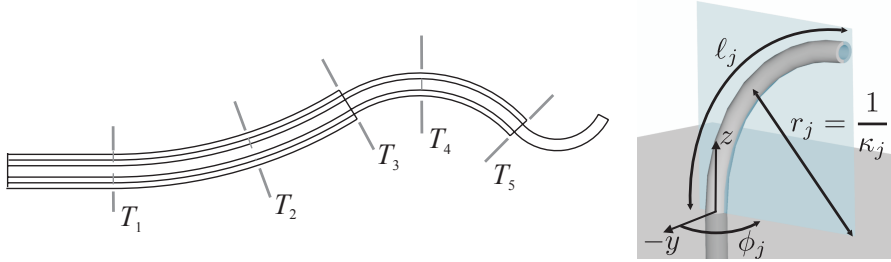
Fig. 2. (Left) The "links," or regions of overlap between component tube transition points, of a three-tube cannula composed of tubes with an initial straight section and a final curved section. Links start and end at transition points, and the jth link is between T_j and T_{j+1}. In this configuration, the largest tube transitions from straight to the left of T_1 to curved to the right. The same is true of the middle tube at T_2 and the smallest tube at T_4. (Right) The arc parameters of a curved link consist of curvature (κ_j), equilibrium plane angle (ϕ_j), and arc length (ℓ_j), as shown. Figures reprinted from [14].

defined by a sequence of unique overlap regions ("links") between transition points T_j, as shown in Figure 2. Each of these remains circular, although bending planes, $\phi(q)$, and curvatures, $\kappa(q)$, change as tubes are axially rotated. The link lengths, $\ell(q)$, are readily determined from the transition point positions in terms of arc length. They are functions of tube base translations, ρ, and the lengths of the straight and curved sections of each tube; an example is given in [15].

The curvatures and planes can be computed as follows. Attach a coordinate frame, T_j, at the base of the link by sliding a copy of the cannula base frame along the backbone (without rotation about z) to the base of the link. The model given in [15] then yields x and y curvature components for the link in the link frame as

$$\chi_j = \frac{\sum_i E_i I_i k_{i,j} \cos\theta_{i,j}}{\sum_i E_i I_i} \quad \text{and} \quad \gamma_j = \frac{\sum_i E_i I_i k_{i,j} \sin\theta_{i,j}}{\sum_i E_i I_i},$$

respectively, where the sums over $i \in \Lambda_j$ only include the tubes that overlap the jth link. The preformed curvature is constant for each tube in each link, and is denoted by $k_{i,j}$ for the ith tube in the jth link. Here, E_i is the elastic modulus, I_i is the cross-sectional moment of inertia, and $\theta_{i,j}$ is the axial i^{th} tube angle about the jth link frame z axis. There is a direct relationship between curvature components and arc parameters, namely

$$\phi_j = \tan^{-1}\left(\frac{\gamma_j}{\chi_j}\right) \quad \text{and} \quad \kappa_j = \sqrt{\chi_j^2 + \gamma_j^2}. \tag{1}$$

Neglecting torsional compliance completely (that is, assuming infinite torsional rigidity), $\theta_{i,j} = \theta_{i,0} \equiv \alpha_i$ for all j, which results in a direct symbolic mapping (1) from actuator space to arc parameters for each link. However,

when transmissional torsion is included, $\theta_{i,1}$ no longer equals actuator input α_i, because the straight transmission will "wind up" as torque is applied at the actuators. Since transmissions are generally long compared to curved sections, we assume that tubes can be modeled as infinitely torsionally stiff beyond T_1, implying that $\theta_{i,j} = \theta_{i,1} \equiv \psi_i$, for all $j > 1$. With these definitions, it is possible to write the total elastic energy of the cannula as a sum of torsional and bending terms,

$$U(\psi_1, \ldots, \psi_n) = \underbrace{\sum_{i=1}^{n} \frac{G_i J_i}{2L_i}(\alpha_i - \psi_i)^2}_{\text{transmission torsion}} + \underbrace{\sum_{j=1}^{m} \sum_{i \in \Lambda_j} \frac{E_i I_i \ell_j}{2}(\chi_j - k_{i,j}\cos(\psi_i))^2}_{x \text{ direction bending}}$$

$$+ \underbrace{\sum_{j=1}^{m} \sum_{i \in \Lambda_j} \frac{E_i I_i \ell_j}{2}(\gamma_j - k_{i,j}\sin(\psi_i))^2}_{y \text{ direction bending}}, \quad (2)$$

where G is the shear modulus, J is the polar moment of inertia, L is the length of straight transmission between actuator and curved section of the tube, and as mentioned previously $i \in \Lambda_j$ are the tubes present in the jth link.

We assume that actuator inputs influence the system quasistatically in the sense that as we move the actuators, the system remains at a local minimum energy. Thus the angles at the end of the straight transmission $(\psi_1, \ldots, \psi_n)$ are always assumed to be at a local minimum of (2). To obtain the minimum of the energy function (2), one can solve for the critical points where the gradient equals zero. This leads to a set of transcendental equations, which can be solved numerically using a variety of techniques, including Newton's method. Further details, including a complete analysis of a three-link example, can be found in [15].

Mapping From Arc Parameters to Shape

The shape of the cannula is defined by the arc parameters and the product of exponentials formula. Let $e_i, i \in \{1, \ldots, n\}$, denote the standard basis for $\mathbb{R}^n$, where $n = 3$ or $n = 6$ will be clear from context. The full kinematics of the mechanism is then given by a product of exponentials:

$$g = g_0 g_1 \cdots g_m, \quad \text{where} \quad g_j = e^{\widehat{e}_6 \Delta\phi_j} e^{(\widehat{e}_3 + \widehat{e}_4 \kappa_j)\ell_j}, \quad j = 1, 2, \ldots, m, \quad (3)$$

$\Delta\phi_j = \phi_j - \phi_{j-1}$, and g_0 is the transformation from the spatial frame to frame 1, which is located at the first transition point. In the following sections we assign the spatial frame to a location on the straight transmission, and the first transition point will be located at a distance ℓ_0 from it. Note that since the transimission is always straight, $\kappa_0 \equiv 0$, $\phi_0 := 0$, and $\Delta\phi_0 := 0$. Thus, in what follows $g_0 = e^{\widehat{e}_3 \ell_0}$. The resulting $g \in \text{SE}(3)$ given in Equation 3 is then the transformation from the spatial frame to the cannula tip.

3.2 Jacobian Computation

Because the transformation g is written directly in terms of the arc parameters, which are, in turn, functions of the joint space, we can conceive of the transformations as a composition of maps, namely $g = g(\boldsymbol{\kappa}(\boldsymbol{q}), \boldsymbol{\phi}(\boldsymbol{q}), \boldsymbol{\ell}(\boldsymbol{q}))$. So, we compute the differential kinematics using the chain rule.

From Arc Space Velocities to End-Effector Velocities

To compute differential kinematics, we begin by computing the spatial velocity (following the notation of [5]) of a single link:

$$\widehat{V}_j = \dot{g}_j g_j^{-1} = \left(\frac{d}{dt} e^{\widehat{e}_6 \Delta\phi_j}\right) e^{(\widehat{e}_3 + \widehat{e}_4 \kappa_j)\ell_j} g_j^{-1} + e^{\widehat{e}_6 \Delta\phi_j}\left(\frac{d}{dt} e^{(\widehat{e}_3 + \widehat{e}_4 \kappa_j)\ell_j}\right) g_j^{-1}$$

$$= \widehat{e}_6 \Delta\dot{\phi}_j + e^{\widehat{e}_6 \Delta\phi_j}\left(\frac{d}{dt} e^{(\widehat{e}_3 + \widehat{e}_4 \kappa_j)\ell_j}\right) g_j^{-1}, \tag{4}$$

where g_j is given in (3).

For ease of exposition, we drop the j subscripts for the following intermediate computations. Let $\widehat{\xi} = \widehat{e}_3 + \widehat{e}_4 \kappa$. Since $e^{\widehat{\xi}\ell}$ varies with both κ and ℓ, the time derivative of the second term in (4) is slightly complicated, but can be written in terms of an infinite series of nested Lie brackets [6]:

$$\frac{d}{dt} e^{(\widehat{\xi}\ell)} = \text{dexp}_{(\widehat{\xi}\ell)}\left(\frac{d}{dt}(\widehat{\xi}\ell)\right) e^{(\widehat{\xi}\ell)}$$

where

$$\text{dexp}_A(C) := C + \frac{1}{2!}[A, C] + \frac{1}{3!}[A, [A, C]] + \dots,$$

and

$$[A, C] := AC - CA.$$

The specific matrices we are interested in here are

$$\widehat{\xi}\ell = \begin{bmatrix} \widehat{e}_1\zeta & e_3\ell \\ 0 & 0 \end{bmatrix} \quad \text{and} \quad \frac{d}{dt}(\widehat{\xi}\ell) = \begin{bmatrix} \widehat{e}_1\dot{\zeta} & e_3\dot{\ell} \\ 0 & 0 \end{bmatrix},$$

where $\zeta = \kappa\ell$. Note that $(\widehat{\xi}\ell)$ and $\frac{d}{dt}(\widehat{\xi}\ell)$ do not commute, so dexp cannot be simplified in the same manner as was possible for the time derivative of the first term in (4). However, it can be simplified by algebraic manipulation to form sine and cosine series as follows. The first few terms are

$$\text{dexp}_{(\widehat{\xi}\ell)}\left(\frac{d}{dt}(\widehat{\xi}\ell)\right) = \begin{bmatrix} \widehat{e}_1\dot{\zeta} & e_3\dot{\ell} \\ 0 & 0 \end{bmatrix} + \frac{1}{2!}\begin{bmatrix} 0 & \widehat{e}_1 e_3\eta \\ 0 & 0 \end{bmatrix} +$$

$$\frac{1}{3!}\begin{bmatrix} 0 & \widehat{e}_1^2\zeta e_3\eta \\ 0 & 0 \end{bmatrix} + \frac{1}{4!}\begin{bmatrix} 0 & \widehat{e}_1^3\zeta^2 e_3\eta \\ 0 & 0 \end{bmatrix} + \dots, \tag{5}$$

where $\eta = \zeta\dot{\ell} - \dot{\zeta}\ell = \kappa\ell\dot{\ell} - \dot{\kappa}\ell\ell - \kappa\ell\dot{\ell} = -\dot{\kappa}\ell^2$. The upper right entry of this matrix can now be manipulated to obtain trigonometric series:

$$
\boldsymbol{e}_3\dot{\ell} + \left(\frac{1}{2!}\widehat{\boldsymbol{e}}_1 + \frac{1}{3!}\widehat{\boldsymbol{e}}_1^2\zeta + \frac{1}{4!}\widehat{\boldsymbol{e}}_1^3\zeta^2 + \dots\right)\boldsymbol{e}_3\eta
$$

$$
= \boldsymbol{e}_3\dot{\ell} + \left[\left(\frac{1}{2!} - \frac{1}{4!}\zeta^2 + \frac{1}{6!}\zeta^4 \pm \dots\right)\widehat{\boldsymbol{e}}_1 + \left(\frac{1}{3!}\zeta - \frac{1}{5!}\zeta^3 + \frac{1}{7!}\zeta^5 \pm \dots\right)\widehat{\boldsymbol{e}}_1^2\right]\boldsymbol{e}_3\eta
$$

$$
= \boldsymbol{e}_3\dot{\ell} + \frac{1}{\zeta^2}\left[(-\cos(\zeta)+1)\,\widehat{\boldsymbol{e}}_1 + (-\sin(\zeta)+\zeta)\,\widehat{\boldsymbol{e}}_1^2\right]\boldsymbol{e}_3\eta
$$

$$
= \boldsymbol{e}_3\dot{\ell} + \frac{1}{\zeta^2}\left[(\cos(\zeta)-1)\,\boldsymbol{e}_2 + (\sin(\zeta)-\zeta)\,\boldsymbol{e}_3\right]\eta.
$$

Applying this in (5), and substituting $\eta = -\dot{\kappa}\ell^2$ from above, results in

$$
\text{dexp}_{(\widehat{\xi}\ell)}\left(\frac{d}{dt}(\widehat{\xi}\ell)\right) = \underbrace{\begin{bmatrix} \widehat{\boldsymbol{e}}_1\dot{\zeta} & \left(\dot{\ell} + \frac{\dot{\kappa}\ell^2(\zeta - \sin(\zeta))}{\zeta^2}\right)\boldsymbol{e}_3 + \frac{\dot{\kappa}\ell^2(1-\cos(\zeta))}{\zeta^2}\boldsymbol{e}_2 \\ 0 & 0 \end{bmatrix}}_{\widehat{A}},
$$

which, when inserted back into (4) yields:

$$
\widehat{V} = \widehat{\boldsymbol{e}}_6\Delta\dot{\phi} + e^{\widehat{\boldsymbol{e}}_6\Delta\phi}\widehat{A}e^{-\widehat{\boldsymbol{e}}_6\Delta\phi}. \tag{6}
$$

To convert this twist in $\mathfrak{se}(3)$ to a vector in $\mathbb{R}^6$ we have $V = \boldsymbol{e}_6\Delta\dot{\phi} + \text{Ad}_{e^{\widehat{\boldsymbol{e}}_6\Delta\phi}}A$. Re-introducing the subscript for the jth link, this reduces to

$$
V_j = \underbrace{\begin{bmatrix} \sin(\Delta\phi_j)(\cos(\kappa_j\ell_j)-1)/\kappa_j^2 & 0 & 0 \\ -\cos(\Delta\phi_j)(\cos(\kappa_j\ell_j)-1)/\kappa_j^2 & 0 & 0 \\ -(\sin(\kappa_j\ell_j)-\kappa_j\ell_j)/\kappa_j^2 & 0 & 1 \\ \cos(\Delta\phi_j)\ell_j & 0 & \cos(\Delta\phi_j)\kappa_j \\ \sin(\Delta\phi_j)\ell_j & 0 & \sin(\Delta\phi_j)\kappa_j \\ 0 & 1 & 0 \end{bmatrix}}_{J_j^s}\begin{bmatrix} \dot{\kappa}_j \\ \Delta\dot{\phi}_j \\ \dot{\ell}_j \end{bmatrix}. \tag{7}
$$

Note that J_j^s is well defined for all $(\kappa_j, \Delta\phi_j, \ell_j)$, even in the the limit as κ_j approaches 0.

Given this "single-link" Jacobian it is straightforward to compute the Jacobian for a multi-link active cannula. All that is necessary is to express the individual link Jacobians in the spatial frame by applying relevant adjoint transformations,

$$
J_{\text{curve}}^s = \begin{bmatrix} J_0 \mid \text{Ad}_{g_0}J_1 \mid \text{Ad}_{g_{01}}J_2 \mid \cdots \mid \text{Ad}_{g_{0(m-1)}}J_m \end{bmatrix} \tag{8}
$$

where J_j is the jth link Jacobian (7), and $g_{0j} = g_0 \cdots g_j$. The computation of V_{st}^s, the spatial velocity of the tool frame, is then a simple matter of stacking

up all m triplets (along with the 0th triplet $\dot{\kappa}_0 \equiv 0$, $\Delta\dot{\phi}_0 \equiv 0$, and $\dot{\ell}_0$ as described in Section 3.1), of arc parameter velocities and multiplying them on the right by the "curve Jacobian" J_{curve}^s in (8).

Some continuum robots permit direct control of arc parameters. With such robots, this result can be directly applied. However, in a robot such as the active cannula where arc parameters are indirectly controlled by joint variables, calculating arc parameter derivatives is more challenging. In an active cannula, a closed-form expression for $\boldsymbol{\kappa}(\boldsymbol{q})$ and $\boldsymbol{\phi}(\boldsymbol{q})$ is generally impossible to compute [15]. However, it is still possible to compute $\dot{\boldsymbol{\kappa}}(\boldsymbol{q})$ and $\dot{\boldsymbol{\phi}}(\boldsymbol{q})$ in closed form, as described below.

Arc Parameter Derivatives

If the system evolves quasistatically (as was assumed in forward kinematics) such that $\boldsymbol{\psi}$ remains at local minimum of $U(\boldsymbol{\psi})$, i.e.

$$\boldsymbol{\psi}^* := \underset{\boldsymbol{\psi}}{\operatorname{argmin}}\, U(\boldsymbol{\psi}),$$

then we can apply the chain rule as follows,

$$\frac{\partial \kappa_j}{\partial \boldsymbol{q}} = \frac{\partial \kappa_j}{\partial \boldsymbol{\psi}^*} \frac{\partial \boldsymbol{\psi}^*}{\partial \boldsymbol{q}},$$

and similarly for ϕ_j. The derivatives of κ_j and ϕ_j with respect to $\boldsymbol{\psi}^*$ are straightforward computations given (1).

We take derivatives of $\boldsymbol{\psi}^*$ with respect to $\boldsymbol{q}$ as follows. We have $\nabla U = F(\boldsymbol{q}, \boldsymbol{\psi}^*) = 0$, and hence

$$D_{\boldsymbol{q}}F = D_1 F + (D_2 F)\,(D_{\boldsymbol{q}}\boldsymbol{\psi}^*) = 0,$$

where $D_1 F$ and $D_2 F$ denote the Jacobian matrix of F with respect to the first and second arguments, respectively. If the Hessian $(D_{\boldsymbol{q}}\boldsymbol{\psi}^*)$ is invertible,

$$D_{\boldsymbol{q}}\boldsymbol{\psi}^* = -(D_2 F)^{-1}(D_1 F).$$

Finally, the computation of $\dot{\ell}_j$ is straightforward. Suppose that a transition point on tube $a \in \{1, \ldots, n\}$ defines the start of link j and a transition on tube $b \in \{1, \ldots, n\}$ defines the end of link j (see Figure 2). Then, the time derivatives of the arc parameters are given by

$$
\begin{aligned}
\dot{\kappa}_j &= -\frac{\partial \kappa_j}{\partial \boldsymbol{\psi}} \left(\frac{\partial F}{\partial \boldsymbol{\psi}^*}\right)^{-1} \frac{\partial F}{\partial \boldsymbol{q}} \dot{\boldsymbol{q}}, \\
\dot{\phi}_j &= -\frac{\partial \phi_j}{\partial \boldsymbol{\psi}} \left(\frac{\partial F}{\partial \boldsymbol{\psi}^*}\right)^{-1} \frac{\partial F}{\partial \boldsymbol{q}} \dot{\boldsymbol{q}}, \\
\dot{\ell}_j &= \dot{\rho}_b - \dot{\rho}_a.
\end{aligned}
\tag{9}
$$

Recalling that $\Delta\phi_j = \phi_j - \phi_{j-1}$, the total Jacobian matrix J_{st}^s in the expression

$$V_{st}^s = J_{st}^s \dot{\boldsymbol{q}} \tag{10}$$

is found by combining (8) and (9).

Fig. 3. Three-tube, six-DOF active cannula actuation unit used in experiments.

4 Empirical Validation via Vision-Based Control

4.1 Position-Based Control Law

Since our initial concern is with linear end effector velocities, we simplify $V_{st}^s = \left(\dot{g} g^{-1} \right)^{\vee} = J_{st}^s \dot{q}$ to obtain an expression for linear velocity, $\dot{p}$, of the cannula tip in world coordinates, as follows. Note that

$$\dot{g} = \begin{bmatrix} \dot{R} \, \dot{p} \\ 0 \; 0 \end{bmatrix} = \widehat{V}_{st}^s g \implies \dot{p} = \omega_{st}^s \times p + v_{st}^s = \begin{bmatrix} I_{3\times 3} \; -\hat{p} \end{bmatrix} V_{st}^s.$$

Recall that n is the number of individual tubes (so there are $2n$ actuated degrees of freedom) and let $J_v, J_\omega \in \mathbb{R}^{3\times(2n)}$ denote the upper and lower three rows, respectively, of J_{st}^s. Then, we have

$$\dot{p} = \begin{bmatrix} I_{3\times 3} \; -\hat{p} \end{bmatrix} \begin{bmatrix} J_v \\ J_\omega \end{bmatrix} \dot{q} = J_p \dot{q}, \tag{11}$$

where $J_p = -\widehat{p} J_\omega + J_v$, and p is the position of the cannula tip in the cannula base frame.

   We apply a simple position-based visual servo scheme. A stereo camera pair triangulates the location of the tip of the cannula in the current image, p, and we drive it to the desired position, p^* via

$$\dot{q} = -J_p^{\dagger} K(p - p^*), \tag{12}$$

where K is a diagonal gain matrix, and p^* is the desired position. Note that we will typically have more than 3 actuated degrees of freedom, which implies that the joint velocities are under determined. Thus, there is freedom in our choice of pseudo-inverse $J_p^{\dagger}$, which may be exploited to accomplish secondary objectives.

   Our experimental system shown in Figure 3 has three actuation stages ($n = 3, m = 5$), but for the experimental results in the subsequent section, we use only two tubes, and hold the first rotation angle constant, thereby reducing J_p to a 3×3 square matrix.
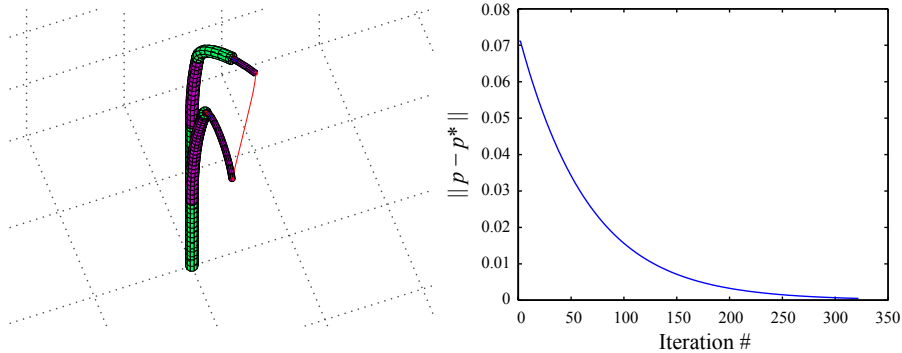
Fig. 4. (Left) A simulated two-tube, three-link (with an initial straight section) active cannula moves in a straight line between two configurations. Colors denote circular arcs or "links". (Right) Tip error as a function of time for the simulation.

4.2 Experimental Results

In the experiments described below we used a two tube, three-link active cannula. Our robotic actuation unit is pictured in Figure 3, and can accommodate up to a three tube, five-link active cannula. Details of the actuation unit are provided in [11]. Our experiments were conducted with the rotation of the outer tube fixed at zero radians as discussed above. An example simulation utilizing the visual servo controller developed in Section 4 is shown in Figure 4. In the simulated, calibrated system, devoid of sensor and motor noise and unmodeled effects, the cannula is capable of servoing to the goal via a straight line trajectory using tip position feedback.

In our experiments, the actuation unit in Figure 3 was commanded by a Linux machine with the RTAI real-time extensions. Low level motor servo loops were run with hard real-time constraints, while the higher level vision-based servo loop was run at the camera frame rate (15 frames per second), without hard real-time consideration. The MATLAB© (The MathWorks Inc., Natick, MA) Engine was used to allow the vision processing software to call the algorithms developed in MATLAB directly. This prototype system allowed rapid development of algorithms. Future work will include porting the validated Jacobian and kinematics algorithms to C++.

To perform the position-based visual servo controller, a calibrated stereo camera system (XCD-X710, Sony, Inc.) was necessary to measure component tube shapes and to triangulate cannula tip position during visual servoing. Camera calibration was performed using the Berkeley Computer Vision Research Group Camera Calibration Toolbox.[5] The transformation from the camera frame to the robot actuation unit base frame was then determined

---

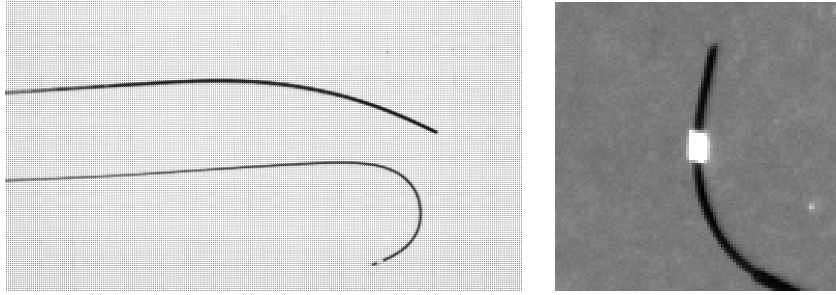[5] http://www.vision.caltech.edu/bouguetj/calib_doc/

Fig. 5. (Left) Experimental component tubes shown disassembled. (Right) Fiducial affixed near the inner tube tip.

using the calibrated cameras. This was accomplished by triangulating points on a grid attached at the cannula base frame.

Component tube curvatures were determined using images of the tubes taken against a physical grid. The grid was used to obtain the mm/pixel ratio, and an automatic fitting procedure was used to find the circle that best fit a large number of points manually tagged as being on the curved tip of the tube. An image used for these measurements is shown in Figure 5-(Left). Lengths of tube straight transmissions were measured using calipers. The physical characteristics of the component tubes are given in Table 1. The inner diameter (ID) and outer diameter (OD) of the tubes were taken from the manufacturer's (Nitinol Devices and Components, Inc., Fremont, CA, USA) specifications. As can be seen in Figure 5-(Left), the heat treatment process used to form the curved shape on the smaller tube produced a near-circular curve with a short straight section near its tip. Rather than cut the tube at this point, we chose to simply attach the fiducial at the end of the circularly curved section as shown in Figure 5-(Right).

A black background in conjunction with a large camera aperture was used to enhance the visibility of the white fiducial. For each camera frame, a sub-window was centered on the position of the cannula fiducial in the previous image. The sub window was thresholded and the center of mass location was taken as the fiducial position measurement in image coordinates. Three-dimensional fiducial coordinates were then triangulated from stereo image coordinates.

Table 1. Component tube physical characteristics.

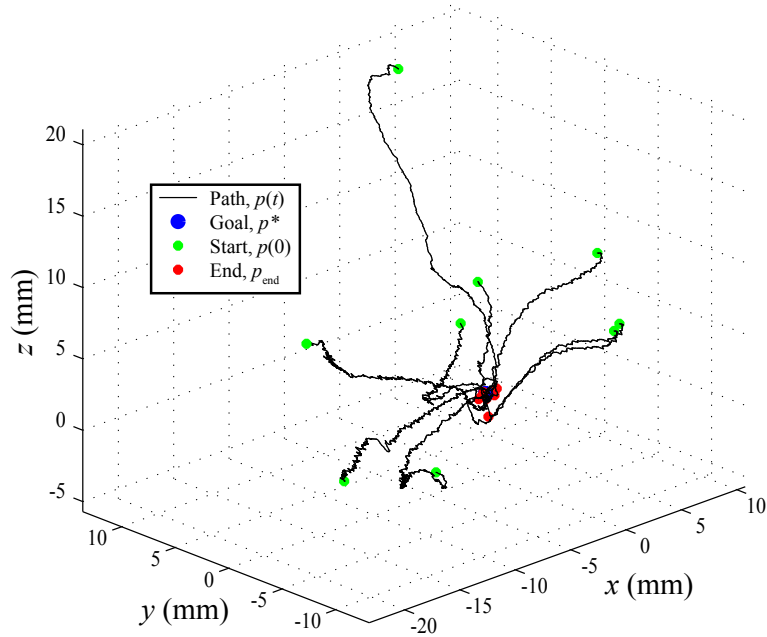|	ID (mm)	OD (mm)	κ (1/m)	l_{curve} (m)	l_{straight} (m)
Inner Tube	0.62	0.80	54.19	0.0571	0.3775
Outer Tube	0.97	1.27	5.97	0.0903	0.0383

Fig. 6. Cannula tip trajectories for a variety of experiments beginning at different initial conditions with initial, final, and goal positions marked. Unfiltered raw data is presented.

The initial conditions of each visual servoing experiment were set away from the workspace boundary. Because of the large curvature of the inner component tube, workspace boundaries in the x and y directions were on the order of ± 1.5 cm, so we explored initial conditions that were approximately 1.0 cm from the goal location. Figure 6 shows a 3D plot of trajectories of the cannula tip for a variety of initial positions. While the active cannula successfully servos to the goal location, note that the trajectories it takes are only approximately rectilinear. There are a number of unmodeled effects and sources of error that contribute to such behavior.

Table 2. Analysis of experimental motions and final displacement errors.

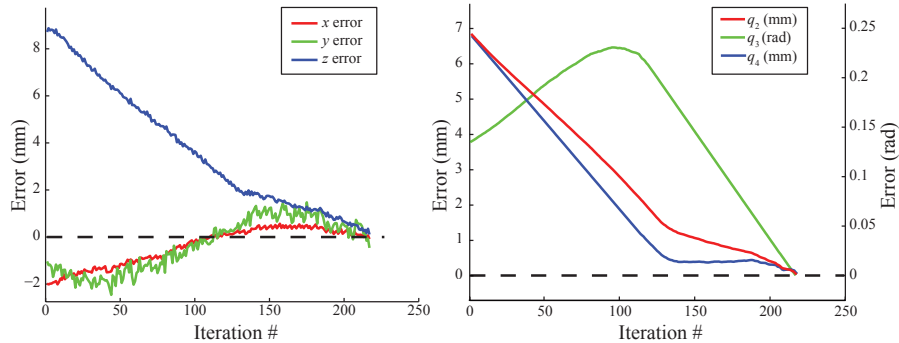| Initial Displacement (mm)		8.80–21.76		
Final Error (mm)	max	1.543		
	avg	0.674		
Per axis final error (mm)		x	y	z
	max	0.822	0.898	1.232
	avg	0.312	0.383	0.324

Fig. 7. Convergence Results: The left images show the cannula tip coordinates as they converge to the goal for a single trial. The right image shows the joint coordinates as they converge to the goal positions over time.

The dominant source of error is likely that these experiments were performed on an uncalibrated cannula. In calculating model parameters, we used manufacturer supplied material properties, some of which have relatively large variances. See [15] for tube property and measurement variances and a statistical analysis of their effects on model parameters. In future work, we plan to implement the calibration methods described in [15], but the fact that visual servoing can be successfully accomplished with an uncalibrated active cannula is noteworthy.

Other sources of error include unmodeled torsion in curved sections of the active cannula (as described in Section 3.1), minor component tube preshaping imperfections, and frictional effects. A small amount of stiction is discernible in the experimental cannula described herein, in contrast to prior larger prototypes where friction has been essentially negligible [15]. This agrees with the intuition that frictional effects should increase as active cannula diameter and intra-tube tolerances decrease. In our experiments, this stiction caused small errors in initial zeroing of the smaller tube rotation angle.

Despite the above-listed sources of error, in our experiments the active cannula always reached a final position less than 2 mm (and typically less than 1 mm) from the goal location. Table 2 provides measurements of maximum and average errors between the goal location and final location of the cannula tip. A typical experiment is shown in Figure 7.

5 Conclusion

The ability of a Jacobian-based visual servo controller to accurately position the active cannula tip is an encouraging result for future active cannula applications. Active cannulas may extend the reach of doctors into new places

in the body, and thereby enable new medical procedures. In minimally invasive surgery, image feedback may be derived from optical stereo endoscopes or other medical imaging modalities. Under all such imaging methods, our visual servoing work should be useful for directing the active cannula accurately through challenging anatomy.

Acknowledgments

References

1. V. K. Chitrakaran, A. Behal, D. M. Dawson, and I. D. Walker. Setpoint regulation of continuum robots using a fixed camera. *Robotica*, 25(5):581–586, 2007.
2. W. Daum. A deflectable needle assembly, 2003. Patent 6,572,593.
3. J. Furusho, T. Katsuragi, T. Kikuchi, T. Suzuki, H. Tanaka, Y. Chiba, and H. Horio. Curved multi-tube systems for fetal blood sampling and treatments of organs like brain and breast. *Journal of Computer Assisted Radiology and Surgery*, pages 223–226, 2006.
4. M. Loser. A new robotic system for visually controlled percutaneous interventions under X-ray or CT-fluoroscopy. Master's thesis, The Albert-Ludwig-University, Freiburg, Germany, September 2002.
5. Richard M. Murray, Zexiang Li, and S. Shankar Sastry. *A Mathematical Introduction to Robotic Manipulation*. CRC Press, Boca Raton, FL, 1994.
6. J. Park and W.-K. Chung. Geometric integration on euclidean group with application to articulated multibody systems. *IEEE Transactions on Robotics*, 21(5):850–863, 2005.
7. G. Robinson and J. B. C. Davies. Continuum robots – a state of the art. *IEEE International Conference on Robotics and Automation*, pages 2849–2854, 1999.
8. P. Sears and P. E. Dupont. A steerable needle technology using curved concentric tubes. *IEEE/RSJ International Conference on Intelligent Robots and Systems*, pages 2850–2856, 2006.
9. P. Sears and P. E. Dupont. Inverse kinematics of concentric tube steerable needles. *IEEE International Conference on Robotics and Automation*, pages 1887–1892, 2007.
10. M. Terayama, J. Furusho, and M. Monden. Curved multi-tube device for path-error correction in a needle-insertion system. *International Journal of Medical Robotics and Computer Assisted Surgery*, 3(2):125–134, 2007.
11. R. J. Webster III. *Design and Mechanics of Continuum Robots for Surgery*. Mechanical engineering, Johns Hopkins University, Baltimore, MD, December 2007. PhD Thesis.
12. R. J. Webster III, J. S. Kim, N. J. Cowan, G. S. Chirikjian, and A. M. Okamura. Nonholonomic modeling of needle steering. *International Journal of Robotics Research*, 25(5/6):509–526, May/June 2006.

13. R. J. Webster III, A. M. Okamura, and N. J. Cowan. Toward active cannulas: Miniature snake-like surgical robots. *IEEE/RSJ International Conference on Intelligent Robots and Systems*, pages 2857–2863, 2006.
14. R. J. Webster III, A. M. Okamura, and N. J. Cowan. Kinematics and calibration of active cannulas. *IEEE International Conference on Robotics and Automation*, pages 3888–3895, 2008.
15. R. J. Webster III, J. M. Romano, and N. J. Cowan. Design and mechanics of active cannulas. *IEEE Transactions on Robotics*, 2008. (Accepted).